Bulletin of the Seismological Society of America, Vol. 76, No. 2, pp. 495–509, April 1986

# LATERAL VELOCITY VARIATIONS IN SOUTHERN CALIFORNIA. I. RESULTS FOR THE UPPER CRUST FROM *Pg* WAVES

BY THOMAS M. HEARN* AND ROBERT W. CLAYTON

## ABSTRACT

**The plate boundary and major crustal blocks in southern California are imaged by a tomographic backprojection of the *Pg* first arrivals recorded by the Southern California Array. The method, formulated specifically for local earthquake arrival times, is a fast, iterative alternative to direct least-squares techniques. With it, we solve the combined problem of determining refractor velocity perturbations and source and station delays. Resolution and variance are found empirically by using synthetic examples.**

**A map showing lateral velocity variations at a depth of approximately 10 km is presented. The results show a strong correlation with surface tectonic features. Clear velocity contrasts exist across the San Andreas, the San Jacinto, and the Garlock faults. The Mojave region has the slowest velocities while the Peninsula Ranges have the highest. The San Jacinto block has velocities intermediate between Mojave and Peninsula Range velocities, and also has early station delays. This may indicate that the San Jacinto block has overridden Mojave material on a shallow detachment surface. No velocity variations are found associated with the Transverse Ranges, which we interpret to mean that the surface batholithic rocks in this area do not extend to *Pg* depths.**

## INTRODUCTION

Determining the depth of crustal geology has been a primary concern of geophysicists. The Southern California seismic array shown in Figures 1 and 2, has provided opportunities to study upper mantle structure (Raikes, 1980; Walck and Minster, 1982; Humphreys *et al.*, 1984; Walck, 1984) as well as Moho structure (Hadley, 1978; Lamanuzzi, 1980; Hearn, 1984b). In this study, the array is used to investigate the structure and velocity variations of the upper crust. The *Pg* first-arrival times recorded on the array are used, since their ray paths bottom in the upper crust. In a companion paper (Hearn and Clayton, 1968; hereafter referred to as HC2), *Pn* waves are used to investigate the velocity variations in the lower crust.

Prior investigations of *Pg* rays in Southern California found velocities of 6.1 to 6.4 km/sec over most of the array (Hadley, 1978). In particular, the Mojave region characteristically displays these slow velocities as does the offshore area (Hadley, 1978; Pechmann, 1983; Corbett, 1984). Another phase, $P*$, is often observed as the first arrival in the Peninsular Ranges at apparent velocities of 6.5 to 6.8 km/sec (Hadley, 1978; Pechmann, 1983). Hadley concluded that this was due to the thinning of a shallow and slower *Pg* layer in the Peninsular Ranges. High $P*$ velocities are also found in the Salton trough. There, metamorphosed sediments form the basement at depths of 5 km with velocities of around 6.0 km/sec, and intruded mafic rocks form a crystalline basement at depths of 13 km (Fuis *et al.*, 1982).

The analysis method used to determine the velocity variations from the travel-time data is presented in the first part of this paper. The results of applying this method to the *Pg* data are shown in the next section, along with a discussion of the

* Present address: Institute for the Study of the Continents, Cornell University, Ithaca, New York, 14853.

resolution and variance of the solution. An interpretation and discussion are given in the final section. The results given here can be compared directly to those given in HC2 for the lower crust.

## TOMOGRAPHY

Tomography is a method that is widely used in medicine for imaging the body. By measuring X-ray attenuation, ultrasonic velocity, or gamma ray intensity, medical technology is able to produce images of body slices, often in real time (Roland, 1979; Deans, 1983). Seismic experiments are substantially different from medicine but many of the same techniques and principles still apply. Geophysical tomography has found application for the whole earth (Dziewonski and Anderson, 1984; Clayton and Comer, 1985; Comer and Clayton, 1985), the upper mantle

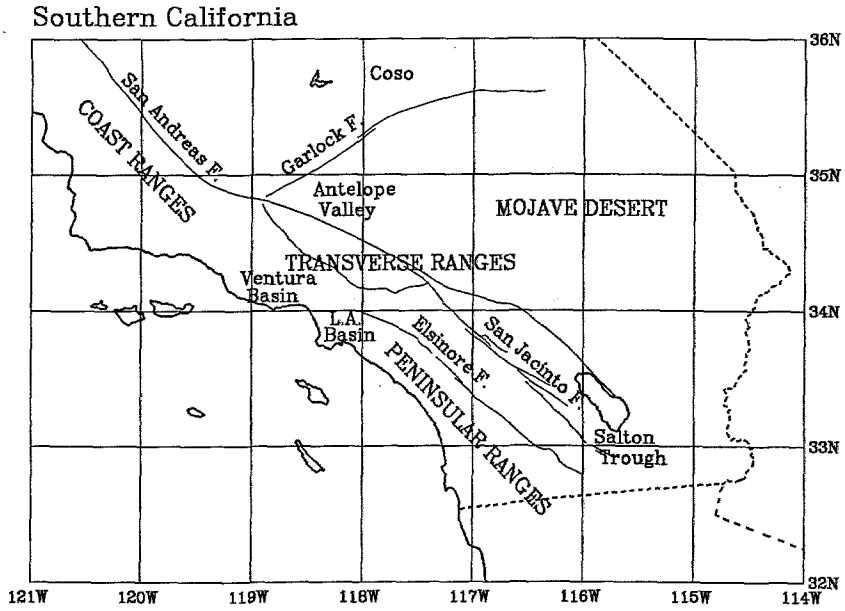


FIG. 1. *Southern California.* The locations of major fault systems and other geographical areas referred to in the text are shown.

(Humphreys *et al.*, 1984), and in seismic exploration (Dines and Lytle, 1979; Fawcett and Clayton, 1984; Menke, 1984). Indeed, many migration and slant stack techniques routinely used in industry are forms of tomography (Deans, 1983). Here, an algorithm developed specifically for refracted crustal arrivals is applied to *Pg* waves by the Southern California array.

The inversion of travel times into structure is the problem of imaging an object from its shadows. Radon (1917) was the first to consider this problem in detail. Travel times are essentially line integrals of the slowness (inverse of velocity) profiles along the ray paths. For a continuous set of shadow data, Radon's theorems show us how to invert uniquely for the image of the object. The Radon transform is a line integral through space of a spatially varying quantity. Its inverses are used directly in medicine where the experiment is well-controlled. Equally spaced data make inverse techniques based on the Radon transform particularly appealing, since

Fast Fourier transform algorithms can be implemented. Bracewell and Riddle (1967) were among the first to make practical application of Radon's work; they used it for imaging the solar corona from fan beam radio telescope data. Since then, modern technology has enabled tomographic techniques to be used for radio astronomy data in astrophysics, occultation data in planetary science, nondestructive testing work in engineering as well as the myriad of medical applications (Rowland, 1979; Deans, 1983).

In the particular application considered here, that of inverting earthquake travel times, there is no choice of location of data points. The distribution of earthquake sources used in this study is shown in Figure 3. The irregular sampling makes direct application of Radon inverses impossible. In addition, the application involves finite path lengths and station and event static corrections, none of which Radon's work encompasses. Because of these complications, the problem is approached through

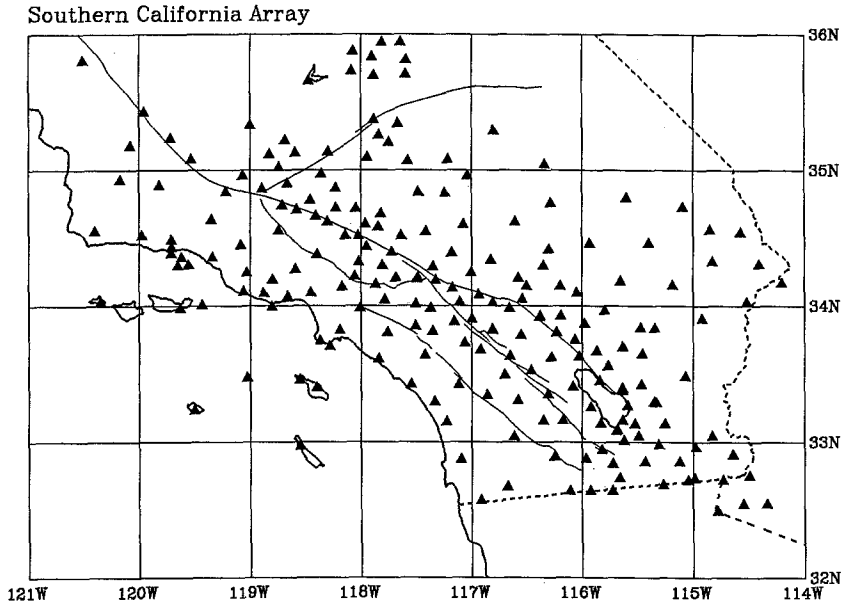


FIG. 2. *The Southern California Array.* The locations of the 160 array stations as of 1983 are shown, along with the major fault systems.

linear inversion theory. Similar approaches in medicine are the Algebraic Reconstruction Technique (ART) and the Kaczmarz method (Rosenfeld and Kak, 1982).

Processing is begun by extracting *Pg* arrivals from the travel-time data. This is done by windowing in time and offset as shown in Figure 4. A straight line is then fit to the data and residuals calculated. The straight line fit is used as the starting model. The intercept time yields the refractor depth; the slope, the slowness. In this starting model, a station elevation correction and an event depth correction are also made. The rest of the processing estimates lateral perturbations in the intercept time and refractor slowness relative to this initial model.

For refracted rays, the time-term model (Scheidegger and Willmore, 1957) provides an equation which separates the residual travel time into three parts corresponding to the source delay, the station delay, and the refraction path between the

source and the receiver. This model is

$$t_{ij} = a_i + b_j + \sum_j d_{ijk} s_k \tag{1}$$

where $t_{ij}$ is the travel time between source $i$ and receiver $j$, $a_i$ and $b_j$ are, respectively, the delays for source $i$ and station $j$, $d_{ijk}$ is the distance the ray travels in block $k$, and $s_k$ is the slowness in block $k$. The station delay can be expressed as a function of refractor depth $h$, refractor slowness $s_0$, and the slowness depth profile, $s(z)$

$$a_i = \int_0^h \sqrt{s(z)^2 - s_0^2}\, dz \tag{2}$$

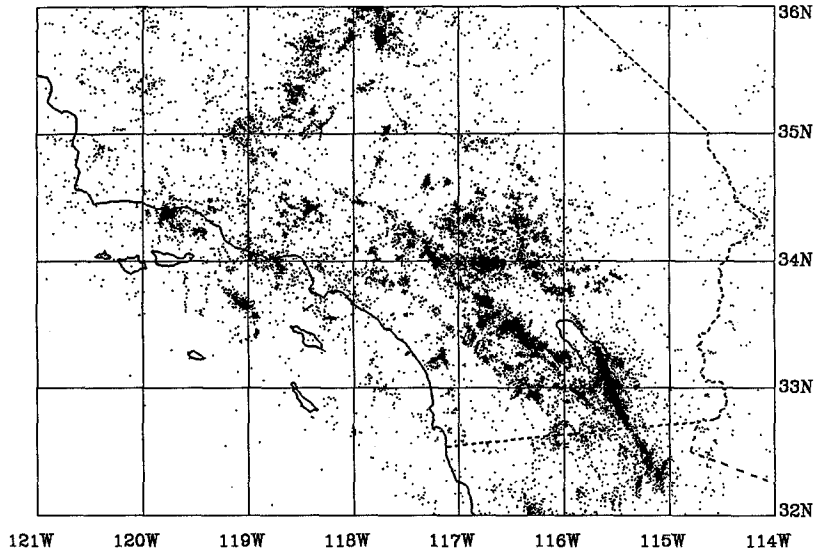


FIG. 3. *Event Locations.* The locations of 44,728 earthquake sources used in this study are shown. These events generate approximately 300,000 usable *Pg* travel-time picks.

which for a constant velocity upper crust reduces to

$$a_i = \sqrt{s^2 - s_0^2}\, h. \tag{3}$$

The event delays have a similar expression with the $h$ replaced by the refractor depth minus the source depth.

To calculate lateral slowness perturbations and crustal delays, we use a tomographic backprojection method that is based on the Jacobi iteration technique. With this technique, the least-squares normal equations are solved via approximating the information matrix by its diagonal elements. With this simple algorithm, the travel times can be processed on a ray-by-ray basis. The travel-time model [equation (1)] can be expressed in a partitioned matrix form as

$$[\boldsymbol{ABC}] \begin{bmatrix} \boldsymbol{a} \\ \boldsymbol{b} \\ \boldsymbol{s} \end{bmatrix} = \boldsymbol{t} \tag{4}$$

where

$\boldsymbol{A}_{li}$ = 1 if arrival $l$ is recorded at station $i$, and 0 otherwise;
$\boldsymbol{B}_{lj}$ = 1 if arrival $l$ is recorded at event $j$, and 0 otherwise;
$\boldsymbol{C}_{lk}$ = the distance ray $l$ travels through cell $k$;
$\boldsymbol{a}$ = the vector of station statics;
$\boldsymbol{b}$ = the vector of event statics;
$\boldsymbol{s}$ = the vector of slowness deviations; and
$\boldsymbol{t}$ = the vector of travel-time residuals.

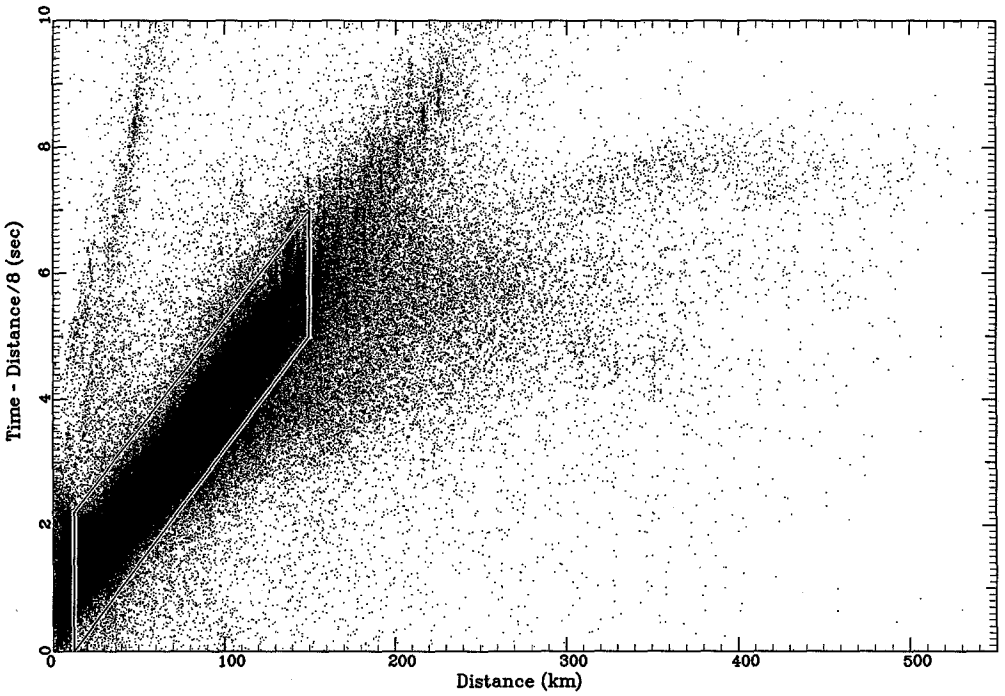


FIG. 4. *Pg Data.* The *P*-wave travel-time picks for 6 yr of array data are shown as a function of source to receiver distance. The picks within the superimposed window are considered to be *Pg* arrivals. In all, over 300,000 *Pg* picks are displayed.

The least-squares solution to this problem can be found by solving the normal equations

$$\begin{bmatrix} \boldsymbol{A}^T\boldsymbol{A} & \boldsymbol{A}^T\boldsymbol{B} & \boldsymbol{A}^T\boldsymbol{C} \\ \boldsymbol{B}^T\boldsymbol{A} & \boldsymbol{B}^T\boldsymbol{B} & \boldsymbol{B}^T\boldsymbol{C} \\ \boldsymbol{C}^T\boldsymbol{A} & \boldsymbol{C}^T\boldsymbol{B} & \boldsymbol{C}^T\boldsymbol{C} \end{bmatrix} \begin{bmatrix} \boldsymbol{a} \\ \boldsymbol{b} \\ \boldsymbol{s} \end{bmatrix} = \begin{bmatrix} \boldsymbol{A}^T\boldsymbol{t} \\ \boldsymbol{B}^T\boldsymbol{t} \\ \boldsymbol{C}^T\boldsymbol{t} \end{bmatrix}. \tag{5}$$

Here, $\boldsymbol{A}^T\boldsymbol{A}$ and $\boldsymbol{B}^T\boldsymbol{B}$ are diagonal matrices with the diagonal elements equal to the number of times a specific station is used or event recorded. The elements of $\boldsymbol{C}^T\boldsymbol{C}$ depend on the ray geometry and the locations of the cells. The diagonal elements

of $C^TC$ give the sum of the squares of the ray segment lengths in cell, while the off-diagonal elements are the cross-products. Almost all of the off-diagonal terms in equation (5) are zero, and the remaining off-diagonal terms are small relative to the diagonal terms. This allows the matrix in equation (5) to be approximated by its diagonal elements. Physically, ignoring the nondiagonal terms corresponds to assuming that each parameter can be estimated independently of the others. The parameter interdependence is resolved by iteration.

Using the diagonal elements of equation (5) and the elements of the right-hand side of equation (5) gives the following estimates for the static delays and the slowness elements.

$$a_i = \sum_j t_{ij}/N_i \tag{6}$$

$$b_j = \sum_i t_{ij}/N_j \tag{7}$$

$$s_k = \frac{\sum_{ij} d_{ijk}^2 (t_{ij}/d_{ijk})}{\sum_{ij} d_{ijk}^2} \tag{8}$$

where $N_i$ and $N_j$ are the number of arrivals at station $i$ and event $j$, respectively. The static delay estimates are thus the mean travel time at each station or event. The slowness estimate for a given cell is simply the average slowness for all rays delayed by that cell weighted by the square of the distance traveled in the cell. The actual algorithm solves on a ray-by-ray basis. Each ray is traced across the grid, and weighted sums are kept for each cell, station, and event involved with that ray. After all of the rays are used, the mean delays and slownesses are calculated. This process is called backprojection, since each travel time is projected back along its ray path. Because data are treated sequentially, there is no limit on the amount of data that can be handled.

After backprojection, the convergence of the algorithm is accelerated by a partial gradient technique. Three scalar factors are determined, one to multiply all the station delays, one to multiply the event delays, and one to multiply the slowness image. The scalars are determined with a three-parameter regression which minimizes the variance of the travel-time residuals. It is in this step that the tradeoff in residual reduction due to the slowness image and the two sets of delays is estimated. After the first estimate of the delays and slownesses is found, a new set of residuals is computed. These residuals are then backprojected, and the resulting slowness perturbations are added to the previous estimate.

The delays computed depend on both the crustal velocity profile and the refractor slowness. Other than the obvious delays caused by the Los Angeles and Ventura basins and the sediments of the Salton trough, there is little knowledge of variations in near-surface velocities. The delays found depend on both the depth of the refractor and the velocity profile above it. Without independent knowledge of crustal velocities, there is little that can be done to separate these two effects.

However, the delay estimates can be corrected for variations in refractor velocity.

Differentiating equation (3) one finds

$$a_i(s_0) = a_i(s_0 + \delta s) - \frac{\partial a}{\partial s_0}\delta s_0$$

$$= a_i(s_0 + \delta s) + s_0 \frac{h}{\sqrt{s^2 - s_0^2}}\delta s$$

$$= a_i(s_0 + \delta s) + F\delta s \tag{9}$$

where $F$ is defined as the offset distance, the horizontal distance that the ray travels from the refractor to the source or station. As this parameter is dependent upon the crustal velocity profile, which is unknown, it will be approximated by a constant value of 23 km. This value assumes an upper crustal velocity of 5.7 km/sec, a refractor velocity of 6.2 km/sec, and a refractor depth of 10 km. All station statics are corrected to the constant value of 23 km.

The corrected delays can be interpreted as either refractor topography or crustal velocity variations. If we assume a constant velocity crust (5.7 km/sec) and 6.2 km/sec refractor at 10 km depth, then 0.1 sec of relative delay corresponds to 1.4 km of refractor topography. If a flat refractor is assumed, then 0.1 sec of relative delay corresponds to 0.12 km/sec upper crustal velocity reduction.

## The Application of Tomography to *Pg* Travel-Time Data

In this study, over 300,000 *Pg* arrivals are used. These were delineated from the rest of the arrivals by plotting the superimposed travel-time plot for all earthquakes that were available from the digital network (Figure 4). The *Pg* branch was then windowed from 15 to 150 km. A line was fit to these data, and outliers of more than 1.1 sec were removed. The data are categorized into five quality levels, depending on the nature of the first arrival. Quality 0 is assigned to sharp impulsive arrivals, while quality 4 denotes poorly picked emergent arrivals. Quality 0, 1, and 2 arrivals were weighted as 400, 100, and 20, respectively. These are the inverses of the estimated variances in travel-time picks. Quality 3 and 4 arrivals were not used. The *Pg* and *P** phases are not separated in the data because only first arrivals are used. Here, *Pg* arrivals are defined as those first arrivals occurring between the direct arrivals at about 15 km distance the *Pn* Moho refractions at about 150 km distance.

The processing is iterative. First the delays, slowness image, and the scaling factors are determined. These effects then are removed from the travel-time data creating a new residual, which in turn is backprojected. All results here are for five iterations. The slowness results for *Pg* are shown at the top of Figure 5, and the associated delays are shown at the bottom. The mean intercept and the inverse slope of the data in Figure 4, after correction for slowness and delay perturbations, are 0.91 sec and 6.2 km/sec, respectively. Assuming a 5.7 km/sec upper crustal velocity and an average event depth of about 5 km, we estimate that the *Pg* rays are bottoming at depths around 10 km. Our velocity structure corresponds to these depths.

The *Pg* velocity range is ±0.69 km/sec but mean velocity perturbations are 0.27 km/sec. The high velocities occur in poorly sampled cells on the edge of the array. This range agrees well with previously observed velocities of 6.0 to 6.8 km/sec

(Hadley, 1978; Pechmann, 1983). The station static delays range over 1 sec. Prominent late delays ocrrespond to the Ventura and Los Angeles basins and the Salton trough where large sections of sediments have accumulated. In order to assess these results more quantitatively, we must look at the quality of the solution.

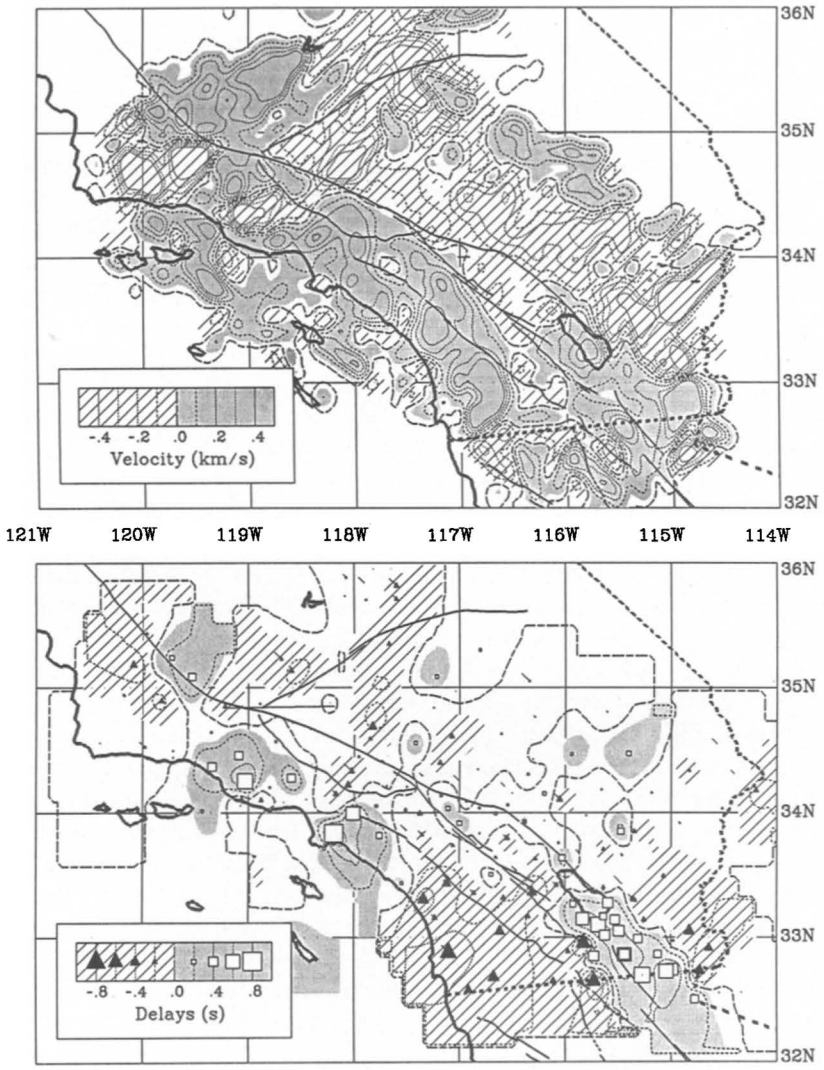


FIG. 5. *Pg Results.* The *upper panel* is a contour plot of lateral variations in *Pg* slowness. The *hatched region* indicates relatively low velocities while the *shaded regions* are relatively fast. The results are strongly correlated with high surface tectonic features such as the San Andreas and Garlock faults. The *lower panel* is a contour plot showing the station delays. The *hatched areas* indicate regions of negative delays or early arrivals. The largest positive delays are associated with the Los Angeles and Ventura basins, and the Salton trough. The largest negative delays occur in the Peninsula Ranges.

## RESOLUTION AND VARIANCE

No inversion study is complete without some discussion of its quality. Here, quality is investigated by empirically determining the resolution and variances of the slowness elements determined. Use of examples generated with synthetic structures and artificial noise make this process simple and easily interpreted.

The effect of noise is found by applying the tomography algorithm to noise alone. Instead of actual travel times, times that have a Gaussian distribution with a standard deviation of 0.055 sec for the highest quality arrivals were used. This is a large amount of error, even when hypocentral mislocations are taken into account. The actual ray paths of the data set were used in the reconstruction. The results of

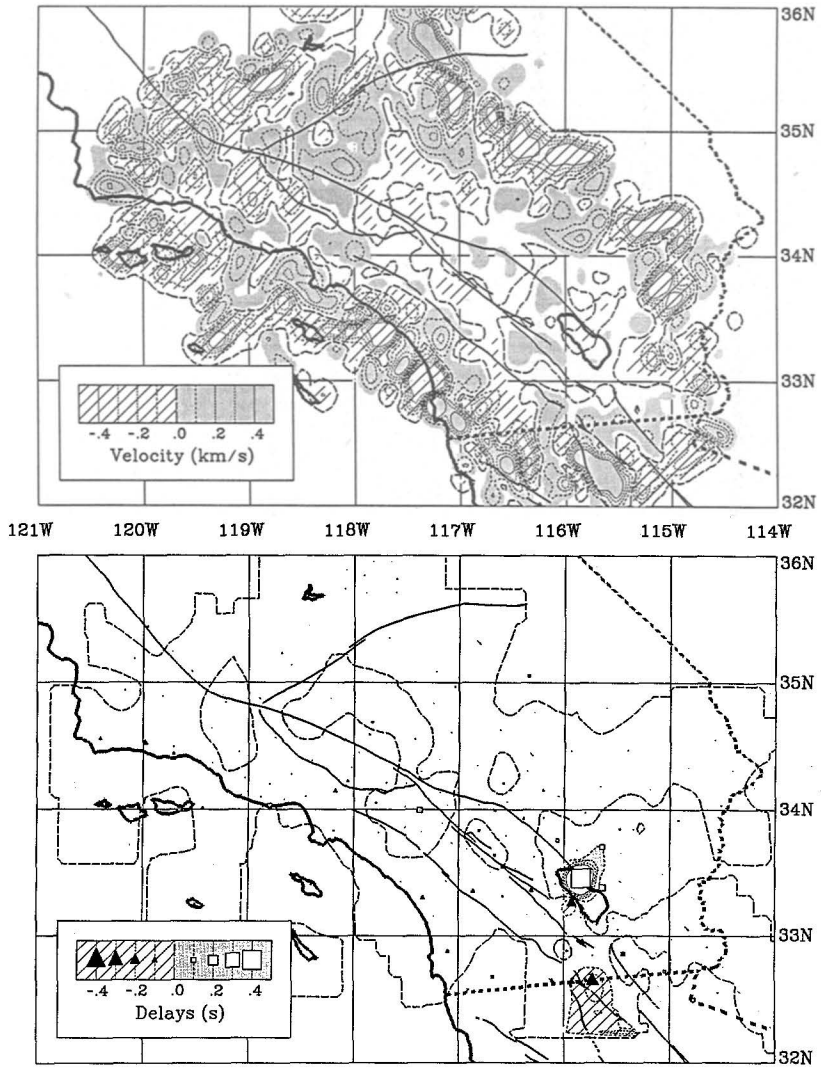


FIG. 6. *Noise Test.* The results of inverting random noise data with a variance similar to the actual data is shown. The *upper panel* gives the slowness results, while the delays are shown in the *lower panel.* The maximum values found are 1.3 km/sec and 0.06 sec. These occur at poorly sampled cells and stations. The ray paths from the real *Pg* data set are used in the inversion.

this are shown at the top of Figure 6. Note that the maximum amplitude produced by this quantity of noise is 1.33 km/sec and that this occurs only on the edge of the region where cells are most poorly sampled. The average noise level is 0.24 km/sec. In the center of the array, the noise amplitude is considerably below the magnitude of the anomalies that are found in the actual *Pg* data. At the bottom of Figure 6,

the delays caused by the noise are shown. The maximum amplitude is 0.06 sec. The largest delays occur at stations that have recorded only a few arrivals.

The apparent resolution of the inversion is also found by considering a synthetic example. Resolution is the degree to which one point in the reconstruction can be distinguished from its neighbors. The resolution of a given slowness element can be found by using a synthetic structure with only that element turned on. Travel times are found using a synthetic structure and the actual ray paths of the data set. This process can give the resolution kernel for any particular element. If this process were to be repeated for all elements, then the equivalent of the resolution matrix that is used in standard inverse theory would be known (Aki and Richards, 1980). Synthetic structures with the *Pg* data set (Hearn, 1984a) indicate resolution widths for individual cells of less than 25 km. The amplitude of the cell is smeared over this width.

As a demonstration of resolution, the tradeoff between delays and slowness perturbations is shown in Figure 7. This tradeoff has proven to be the most difficult problem with the data. It is inherently difficult to tell whether late arrivals are due to a static source or receiver delay, or due to a localized velocity anomaly. This is attributed to nonuniqueness in the data and not the tomographic method used. More standard matrix methods would encounter near-zero eigenvalues which imply a nonuniqueness in the solution. The synthetic structure chosen has horizontal bars of constant slowness alternating vertically across the array and vertical bars of constant event and station delay alternating horizontally across the array. This structure is substantially more difficult to resolve than that encountered for Southern California. Again, the actual ray paths of the data set are used. Examination of Figure 7 shows that some tradeoff exists but the main pattern is quite clear. The individual station responses show little tradeoff with the slowness image but the constructive interference of several close stations is capable of distorting the slowness image. The input amplitudes were $\pm 0.15$ sec and $\pm 0.20$ km/sec for the delays and slowness, respectively. The average amplitude of the reconstructed delay stripes is correct but individual stations have errors of up to 0.2 sec. The slowness stripes here have maximum amplitudes that are too high by a factor of almost three but the mean amplitude of 0.27 km/sec is close to the input amplitude.

The slowness image for Southern California (Figure 5, top) shows many streaking artifacts that are also apparent in the synthetic stripe model image (Figure 7, top). One artifact is due to azimuth bias in certain regions, when the ray paths are predominantly from one azimuth and the velocity perturbations are spread out along that azimuth. Again, this is a problem with the data distribution and not with the method. Tomography produces the recognizable artifact of streaking in poorly resolved areas.

Streaking is particularly obvious from the Coso area (35.7°N, 117.6°W) where a large number of events and stations are located. Cells on the northeast side of the image are sampled predominantly by ray paths from Coso, causing streaking in the northwest direction. Since typical resolution widths are on the order of 25 km, some of the smaller features in the slowness image may be spurious, particularly those on the edge where the noise level is higher.

As the solution found for Southern California is much smoother than the striped model, we feel that the delays found are good within 0.2 sec. Comparison of the slowness image with the delays (Figure 5). shows little consistent correlation between the delays and slownesses. Judging from the synthetics, the larger features of the slowness image have the correct mean amplitude but the extreme points are

probably correct only within a factor of three. The results show much larger amplitudes than were found earlier by Ergas and Jackson (1981), who used a much poorer data set. They had removed station delays by removing their average residual prior to estimating the slowness. Our experience has found that static delays

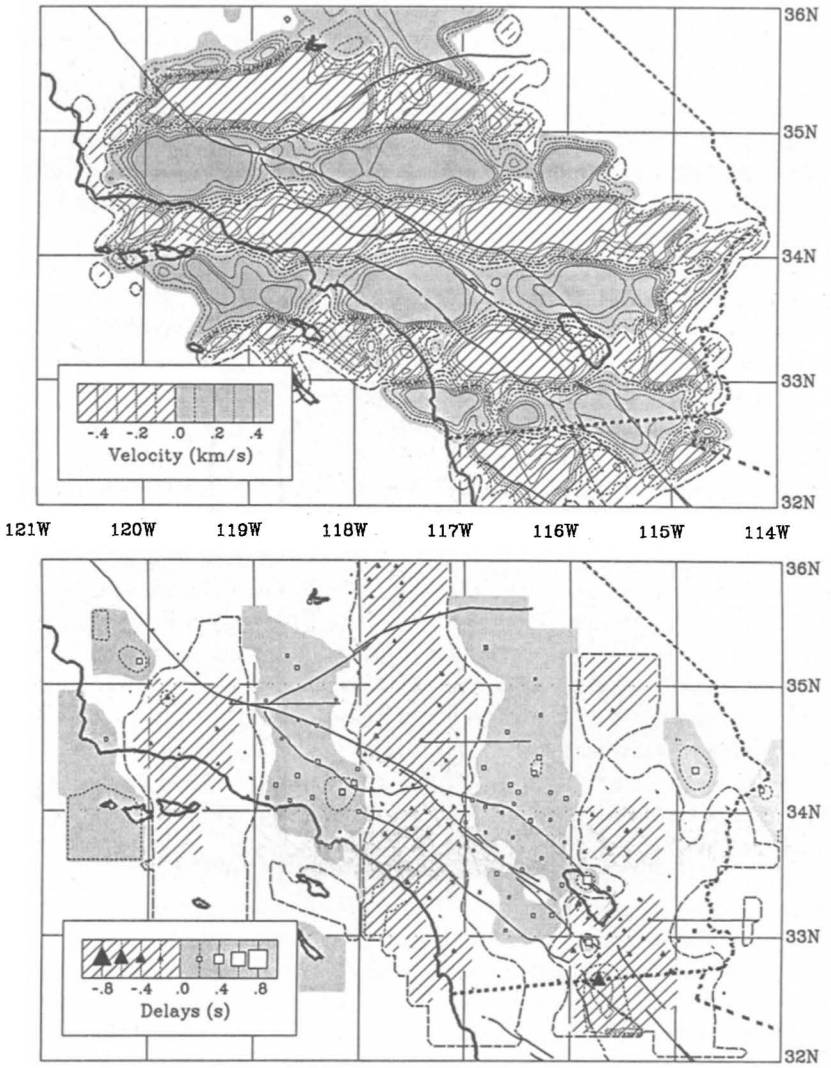


FIG. 7. *Test Pattern.* The results of inverting the striped model synthetic are shown. The model consists of alternating horizontal stripes of slowness variations, combined with alternating vertical stripes of delays. The synthetic is designed to show the coupling between the slowness and delay part of the solution. The input amplitudes were ±0.2 km/sec and ±0.15 sec. The *upper panel* gives the slowness results, while the delays are shown in the *lower panel.* The ray paths of the real *Pg* data set are used in the inversion.

contribute as much to the residual as do the slowness variations; therefore, they must be explicitly included as part of the problem.

## DISCUSSION

The San Andreas fault system is spectacularly imaged at the top of Figure 5. The San Andreas is particularly apparent south of the Garlock fault to the Coachella

Valley region. Rocks on the Pacific plate are faster with velocities near 6.6 km/sec. Rocks on the opposite plate have velocities of less than 6.0 km/sec. Also nicely outlined are the westernmost Garlock fault and the northern San Jacinto fault. The intersection of the Garlock fault and the San Andreas fault outlines the Antelope Valley region. Similarly, the corner between the San Andreas and the San Jacinto faults is well outlined. Comparison with the gravity of Southern California (Oliver, 1982) shows many of these same features. Low-velocity values in the Mojave directly correspond to low gravity values there.

The associated delays (Figure 5, bottom) show little of the tectonic correlations seen in the slowness image. Instead, the delays are dominated by sediment delays in the Ventura and Los Angeles basins and the Salton trough. Excluding those areas, the delays vary on average about ±0.3 sec. This could correspond to as much as ±4.2 km refractor topography in the absence of upper crust velocity variations.

Impressively, the mid-crustal velocities do not seem to see either the San Gabriel Ranges or the San Bernardino Ranges. Resolution quality in the Ranges is quite good as seen by the clearness of the San Andreas in Cajon Pass. Both of the batholiths are more dense and thus presumably faster than the Mojave region. Yet neither of the batholiths show up as a unit at *Pg* depths. Instead, the San Bernardino Mountains seem to have Mojave-type velocities. One would expect the San Gabriels to have a velocity intermediate between the Mojave and the Peninsular Ranges, instead they are not seen as a unit, but have velocities nearing the Peninsular Range velocity. It seems that these large batholiths do not exist clearly at depths of 10 km.

Evidence shows that most of the province has been displaced. There are 90° rotations in the rocks of the westernmost Transverse Ranges (Luyendyk *et al.*, 1980). The San Andreas clearly cuts through the Transverse Ranges at *Pg* depths. The San Gabriel and San Bernardino mountains could not have formed as a continuous structure, given 300 km of fault offset; the present juxtaposition is primarily coincidence. Indeed, Powell (1981) has shown that the San Gabriels have moved from analogous terrain south of the San Bernardino Mountains in the Mojave Desert. No root is apparent for the San Gabriels and, at most, a 8 km root exists for the San Bernardinos, far less than that predicted by isostasy (Lamanuzzi, 1981; Hearn, 1984).

Displacement of the San Bernardino Mountains could be accomplished by a large detachment surface at shallow depths. The shallow seismicity base of 5 to 10 km in the Mojave and underneath the San Bernardinos supports the case for a shallow ductile to brittle transition and could be a good site for detachment faulting (Corbett, 1984). The Transverse Range province, though, contains more than the San Gabriel and San Bernardino batholith complexes. The Santa Monica Mountains, Santa Ynez Mountains, and the Channel Islands are also included in this high relief province. The batholiths of the Transverse Ranges are allochtonous surficial features. The granitic material and other rocks of the Transverse Ranges have piled up on the earth's surface in the convergent zone of the big bend area of the San Andreas fault but are not present at depth.

The only part of the Transverse Range area that has anomalous slowness values is the north Ventura Basin. Comparison with the static delays shows large delays for the same area. The sediments of Ventura cause both slow velocities and late arrivals. In contrast, note that the Los Angeles basin shows up only in the static delays, as does the Salton trough. The slow velocities pictured near Ventura are real and are due to ray paths that actually traverse this deep basin.

The Tehachapi Range forms the southernmost tip of the Sierran batholith. It is bounded on the south by the Garlock fault. Although the Sierras and the Owens Valley region show slower, Mojave-type velocities, the Tehachapies show faster velocities. The Tehachapi Range, then, may be similar to the Transverse Ranges where the granitic rocks are surficial and the topographic high is due to convergence in the big bend area. The westward bend of this southern Sierran tip may indicate that these rocks have been dragged by left-lateral movement on the Garlock fault.

In contrast to the southern Sierran tip and the Transverse Ranges, the Peninsular Ranges do seem to extend to *Pg* refractor depths. High-velocity refractors have been noted here before (Simmons, 1977; Hadley, 1978). Also, the tonalites of the Peninsular Ranges have extremely high densities, some up to 2.85 gm/cm$^3$ (Silver, personal communication). Velocities here are from ray paths either refracting through the batholith or along its base. The delays show no evidence for the refractor being deeper there. In fact, along the coast they show evidence for a shallower refractor. Perhaps the base of the batholith becomes shallower along this edge. If we assume higher crustal velocity of 6.2 km/sec instead of 5.7 km/sec and a refractor velocity of 6.5 km/sec there, the time delay due to 5 km of fast overburden is −0.18 sec. In terms of depth, this could add 2.5 km more to a depth estimate there.

The San Jacinto block, the portion of the Peninsula Ranges wedged between the San Andreas and the San Jacinto faults, has a different, lower velocity character than the rest of the Peninsular Ranges. It seems to be more closely associated with Mojave velocities. It also seems to have early delays of 0.2 sec indicating a refractor 3 km shallower there. The 30 km of offset on the San Jacinto fault is too small to cause the velocity pattern seen. As the Peninsular Ranges have moved up against the big bend area, the San Jacinto block may have overridden the opposite plate. This would have aided in the development of a surficial bend in the San Andreas and helped create the tremendous elevation of San Jacinto Peak. The plate boundary, past or present, in the mid-crust could cut directly underneath the San Jacinto fault from Cajon Pass to the Salton trough. The San Jacinto fault has only 30 km of displacement and could be a late developing response to such thrusting.

The Mojave Desert region, particularly in the Antelope Valley area, shows a characteristic velocity of less than 6.0 km/sec. These low velocities extend into Arizona (Warren, 1969; Sinno *et al.*, 1981). Similar velocities also can be found in the Gabilan Range of central California, displaced in a right-lateral sense from the Mojave. The displacement, which is poorly constrained, seems larger than the 300 km of San Andreas offset.

South of the Salton Sea is an area of very high apparent *Pg* velocity. This result is corroborated by the high-apparent *Pg* velocities (up to 7.0 km/sec) that are observed from events in that area. Also, Fuis *et al.* (1982) find high velocities there. They interpret these as layers of metamorphosized sediments and intruded volcanic material. Their 7.0 km/sec layer is at the shallow depth of 13 km. The large delays that are seen here (0.2 to 0.5 sec) are due to the sediments on the valley's surface.

## CONCLUSIONS

Tomographic backprojection is an efficient and effective method for investigating crustal structure. Here, tomographic backprojection is extended to include station and event static delays. By using this method for the *Pg* arrivals of the Southern California array, the major crustal blocks of Southern California are clearly outlined.

The boundaries of these blocks correspond with the fault zones of the San Andreas fault, the Garlock fault, and the San Jacinto fault. Lower velocities are in the Mojave region and higher velocities are in the Peninsular Ranges and the southern Salton trough.

Many of the features observed are quite different from their surface expressions. The Transverse Ranges are not seen and neither is the Tehachapi Range. This suggests that these batholiths are only surficial. The San Jacinto block has a shallower refraction depth and velocities more akin to the slow Mojave than the faster Peninsular Ranges. The block has perhaps overridden Mojave material.

## ACKNOWLEDGMENTS

This study was supported by a research contract with the U.S. Geological Survey (14-08-001-21210) and a grant from the Sun Oil Company. Part of the graphics and computing facilities used in this study were provided by the W. M. Keck Foundation. We thank Eugene Humphreys, Leon Silver, and Hiroo Kanamori for their suggestions and reviews.

## REFERENCES

Aki, K. and P. G. Richards (1980). *Quantitative Seismology*, Vol. 2, W. H. Freeman and Company, San Francisco, California.

Bracewell, R. N. and A. C. Riddle (1967). Inversion of fan beam scans in radio astronomy, *Astrophys. J.* **150,** 427–434.

Clayton, R. W. and R. P. Comer (1985). Reconstruction of mantle heterogeneity by iterative backprojection of travel times. 2. Results for *P* waves (submitted for publication).

Comer, R. P. and R. W. Clayton (1985). Reconstruction of mantle heterogeneity by iterative backprojection of travel times. 1. Theory and reliability (submitted for publication).

Corbett, E. J. (1984). Seismicity and crustal structure studies of Southern California: tectonic implications from improved earthquake locations, *Ph.D. Thesis*, California Institute of Technology, Pasadena, California.

Deans, S. R. (1983). *The Radon Transform and Some of its Applications*, John Wiley and Sons, New York, New York.

Dines, K. A. and R. J. Lytle (1979). Computerized geophysical tomography, *Proc. IEEE* **67,** 1067–1073.

Dziewonski, A. M. and D. L. Anderson (1984). Seismic tomography of the earth's interior, FIAmerican Scientist, 483–494, Sept.–Oct.

Ergas, R. A. and D. D. Jackson (1981). Spatial variations of crustal seismic velocities in Southern California, *Bull. Seism. Soc. Am.* **71,** 671–689.

Fawcett, J. A. and R. W. Clayton (1984). Tomographic reconstruction of velocity anomalies, *Bull. Seism. Soc. Am.* **74,** 2201–2219.

Fuis, G. S., W. D. Mooney, J. H. Healy, G. A. McMechan, and W. J. Lutter (1982). Crustal structure of the Imperial Valley Region, in *The October 15, 1979 Imperial Valley Earthquake, U.S. Geol. Surv. Profess. Paper 1254*, 25–50.

Hadley, D. (1978). Geophysical investigations of the structure and tectonics of Southern California, *Ph.D. Thesis*, California Institute of Technology, Pasadena, California.

Hearn, T. M. (1984a). Crustal structure in Southern California from array data, *Ph.D. Thesis*, California Institute of Technology, Pasadena, California.

Hearn, T. M. (1984b). *Pn* travel times in Southern California, *J. Geophys. Res.* **89,** 1843–1855.

Hearn, T. M. and R. W. Clayton (1986). Lateral velocity variations in Southern California. II. Results for the lower crust from *Pn* waves, *Bull. Seism. Soc. Am.* **76,** 511–520.

Humphreys, E., R. W. Clayton, and B. H. Hager (1984). A tomographic image of mantle structure beneath Southern California, *Geophys. Res. Letters* **11,** 625–627.

Lamanuzzi, V. (1981). Relative *Pn* travel time residuals for stations in Southern California, *Master's Thesis*, University of Southern California, Los Angeles, California.

Luyendyk, B. P., M. J. Kamerling, and R. Terres (1980). Geometric model for Neogene crustal rotations in Southern California, *Geol. Soc. Am. Bull.* **91,** 211–217.

Menke, W. (1984). The resolving power of cross-borehole tomography, *Geophys. Res. Letters* **11,** 105–108.

Oliver, H. W. (1982) (Editor). Interpretation of the gravity map of California and its continental margin, *Calif. Div. Mines Geol. Bull.* 205.

Pechmann, J. C. (1983). The relationship of small earthquakes to strain accumulation along the San Andreas Fault, *Ph.D. Thesis*, California Institute of Technology, Pasadena, California.

Powell, R. E. (1981). Geology of the crystalline basement complex, eastern Transverse Ranges, Southern California: constraints on regional tectonic interpretation, *Ph.D. Thesis*, California Institute of Technology, Pasadena, California.

Radon, J. (1917). A translation of Radon's 1917 paper, in *The Radon Transform and Some of its Applications*, by S. R. Deans, John Wiley and Sons, New York, 204–217.

Raikes, S. A. (1980). Regional variations in upper mantle structure beneath Southern California, *Geophys. J. R. Astr. Soc.* **63,** 187–216.

Roland, S. W. (1979). Computer implementation of image reconstruction formulas, in *Image Reconstruction from Projections*, G. T. Herman, Editor, Springer-Verlag, Berlin.

Rosenfeld, A. and A. C. Kak (1982). *Digital Picture Processing*, Vol. 1, Academic Press, New York.

Scheidegger, A. E. and P. L. Willmore (1957). The use of a least squares method for the interpretation of data from seismic surveys, *Geophysics* **22,** 9–22.

Simmons, R. S. (1977). Seismicity of San Diego, 1934–1974, *Bull. Seism. Soc. Am.* **67,** 809–826.

Sinno, Y. A., G. R. Keller, and M. L. Sbar (1981). A crustal seismic refraction study in west central Arizona, *J. Geophys. Res.* **86,** 5023–5038.

Walck, M. C. and J. B. Minster (1982). Relative array analysis of upper mantle velocity variations in Southern California, *J. Geophys. Res.* **87,** 1757–1772.

Walck, M. C. (1984). Teleseismic array analysis of upper mantle compressional velocity structure, *Ph.D. Thesis*, California Institute of Technology, Pasadena, California.

Warren, D. H. (1969). A seismic-refraction survey of central Arizona, *Geol. Soc. Am. Bull.* **80,** 257–282.

SEISMOLOGICAL LABORATORY
CALIFORNIA INSTITUTE OF TECHNOLOGY
PASADENA, CALIFORNIA 91125
CONTRIBUTION NO. 4195

Manuscript received 6 August 1985